



# Magnetic Structure of a Composite Solar Microwave Burst

Jeongwoo Lee<sup>1,2</sup> , Stephen M. White<sup>3</sup> , Chang Liu<sup>1</sup> , Bernhard Kliem<sup>2,4</sup> , and Satoshi Masuda<sup>2</sup>

<sup>1</sup>Space Weather Research Laboratory, New Jersey Institute of Technology, Newark, NJ 07102, USA; [leej@astro.snu.ac.kr](mailto:leej@astro.snu.ac.kr)

<sup>2</sup>Institute for Space-Earth Environmental Research, Nagoya University, Aichi 464-8601, Japan

<sup>3</sup>Air Force Research Laboratory, Space Vehicles Directorate, Albuquerque, NM, USA

<sup>4</sup>Institute of Physics and Astronomy, University of Potsdam, Potsdam D-14476, Germany

Received 2017 September 28; revised 2018 February 5; accepted 2018 February 5; published 2018 March 26

## Abstract

A composite flare consisting of an impulsive flare SOL2015-06-21T01:42 (*GOES* class M2.0) and a more gradual, long-duration flare SOL2015-06-21T02:36 (M2.6) from NOAA Active Region 12371, is studied using observations with the Nobeyama Radioheliograph (NoRH) and the *Solar Dynamics Observatory* (*SDO*). While composite flares are defined by their characteristic time profiles, in this paper we present imaging observations that demonstrate the spatial relationship of the two flares and allow us to address the nature of the evolution of a composite event. The NoRH maps show that the first flare is confined not only in time, but also in space, as evidenced by the stagnation of ribbon separation and the stationarity of the microwave source. The NoRH also detected another microwave source during the second flare, emerging from a different location where thermal plasma is so depleted that accelerated electrons could survive longer against Coulomb collisional loss. The AIA 131 Å images show that a sigmoidal EUV hot channel developed after the first flare and erupted before the second flare. We suggest that this eruption removed the high-lying flux to let the separatrix dome underneath reconnect with neighboring flux and the second microwave burst follow. This scenario explains how the first microwave burst is related to the much-delayed second microwave burst in this composite event.

**Key words:** Sun: activity – Sun: coronal mass ejections (CMEs) – Sun: flares – Sun: magnetic fields – Sun: radio radiation – Sun: UV radiation

**Supporting material:** animations

## 1. Introduction

Understanding how the solar magnetic field releases energy during flares is one of the most important topics of solar physics. A primary task is to determine the timing and location of flare energy release and the coronal magnetic structure for a given photospheric magnetic structure of erupting active regions. While  $H\alpha$  images of the chromosphere and extreme ultraviolet (EUV) images of corona are often used for this purpose, hard X-rays and microwaves provide information on the primary energy release in the form of high-energy electrons accelerated during solar flares. Early hard X-ray observations brought up the notion of impulsive (Wild et al. 1963) and gradual (Kane 1969) flares. Impulsive flares show simple loop systems without a cusp structure in soft X-rays, as found by *Skylab* and *Yohkoh*, and hence they are also often called compact flares or confined flares (Pallavicini et al. 1977). Historically, impulsive flares were considered to release energy inside the loop observed in soft X-rays (Alfvén & Carlqvist 1967; Uchida & Shibata 1988). On the other hand, if the energy is released outside the loop in a current sheet above the soft X-ray loop, the flares then tend to be of long duration as the reconnection can proceed to large heights; these are called eruptive flares if associated with a coronal mass ejection (CME) (Shibata & Magara 2011). While the long-duration flare may imply a slow rise followed by a slow decay (i.e., a gradual flare lacking an impulsive rise phase), some of the eruptive flares can rapidly rise followed by long decay, also called long-duration events (LDE).

Kosugi et al. (1988) carried out a comprehensive study of the impulsive and extended flares using 400 events observed by the hard X-ray burst spectrometer on board the *Solar Maximum*

*Mission* (SMM) satellite and the Nobeyama 17 GHz radiometer to find that impulsive bursts tend to be X-ray-rich and extended bursts are microwave-rich. They also found cases in which an impulsive component is followed by a secondary component that has a longer characteristic timescale. Such events (hereafter called “composite” flares) have not received much attention (Bai & Sturrock 1989), and are described as a main flare followed by either post-burst-increase (Kosugi et al. 1983); late-phase gradual enhancements in microwaves and hard X-rays (Kai et al. 1983); or a delayed acceleration process (Nakajima et al. 1985; Kai et al. 1986). The contrasting behaviors of the preceding and following flares might imply one common acceleration mechanism with two different trapping conditions for accelerated electrons or, alternatively, two different acceleration mechanisms in one or two different sources. Any causal relation between the two phases is potentially important for understanding flares. Obviously, it is hard to resolve these issues with time profiles and spectra alone. The locations of accelerated electrons can be identified in hard X-ray and/or microwave images; here, we study microwave observations of a composite flare that demonstrate this causal relationship.

In this paper, we study a composite flare on 2015 June 21 with high-resolution imaging data from the Nobeyama Radioheliograph (NoRH) and the *Solar Dynamics Observatory* (*SDO*). We start from the common notion that impulsive flares tend to be confined, and long-duration flares are typically eruptive (i.e., associated with CMEs). Although there is a broad range of durations where both forms occur in about equal proportion (Andrews 2003), the statistical trend of the longer duration of flares associated with CMEs than that of flares without CMEs is clearly identified (Yashiro et al. 2006). We

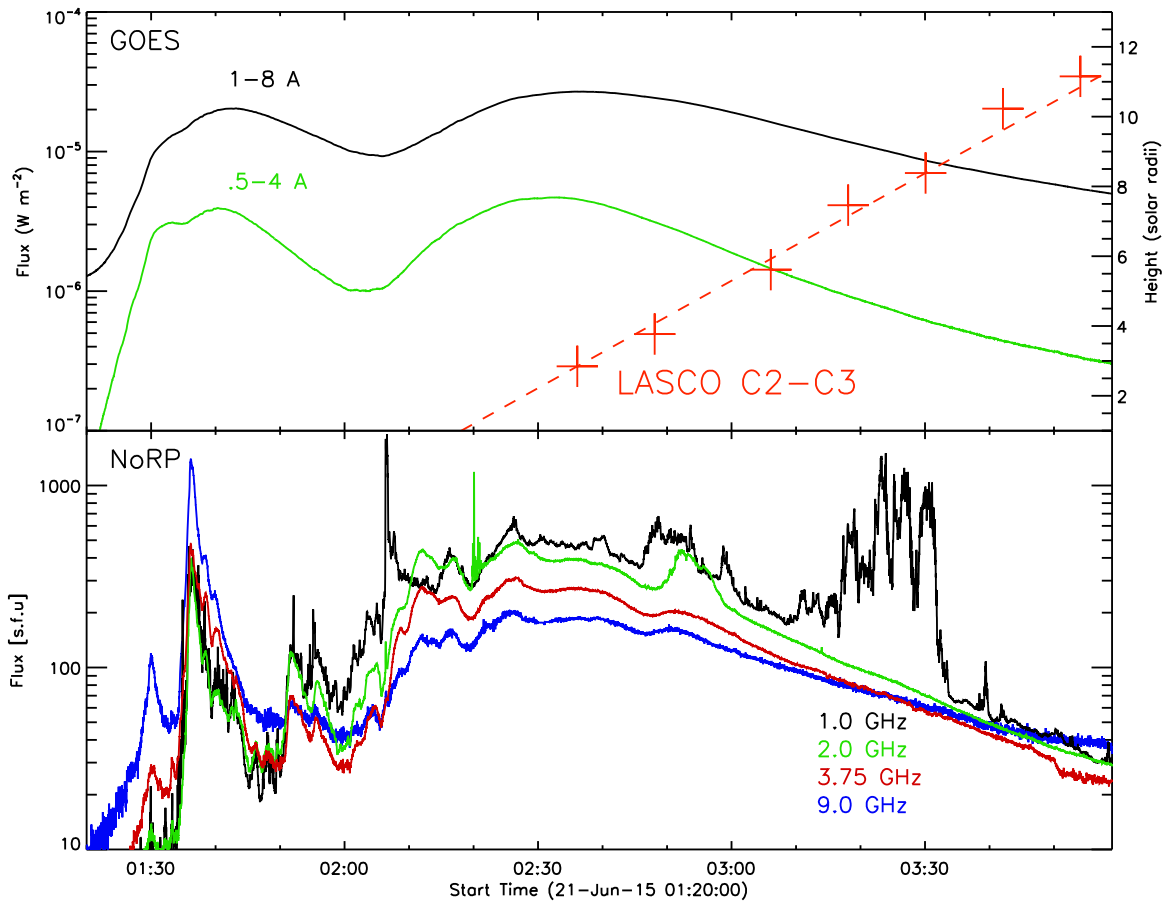


**Figure 1.** Light curves of *GOES* soft X-rays (top) and the NoRP microwaves (bottom) during the 2015 June 21 flare. The cross symbols with a linear fit represent the CME front detected by the LASCO C2 and C3 telescopes.

investigated the nature of the impulsive and the long-duration components in this composite event, and will show that the deduced scenario is more complicated than the simple paradigm of confined versus eruptive flares. In addition, we found an unusual, second nonthermal microwave source in the long-duration event, and we will discuss how such a new source can be understood. A related investigation (Kliem et al. 2018) focuses on the formation of a magnetic flux rope, observed as an EUV hot channel, by the impulsive flare.

The sections of this paper are as follows. Time profiles of the microwave and X-ray fluxes are presented in Section 2. We compare the microwave maps from the NoRH with the (E)UV images obtained with the *SDO* Atmospheric Imaging Assembly (AIA; Lemen et al. 2012) images in Section 3. We then interpret the observational results based on the magnetic structure of the active region reconstructed using the nonlinear force-free field (NLFFF) model in Section 4, and conclude in Section 5.

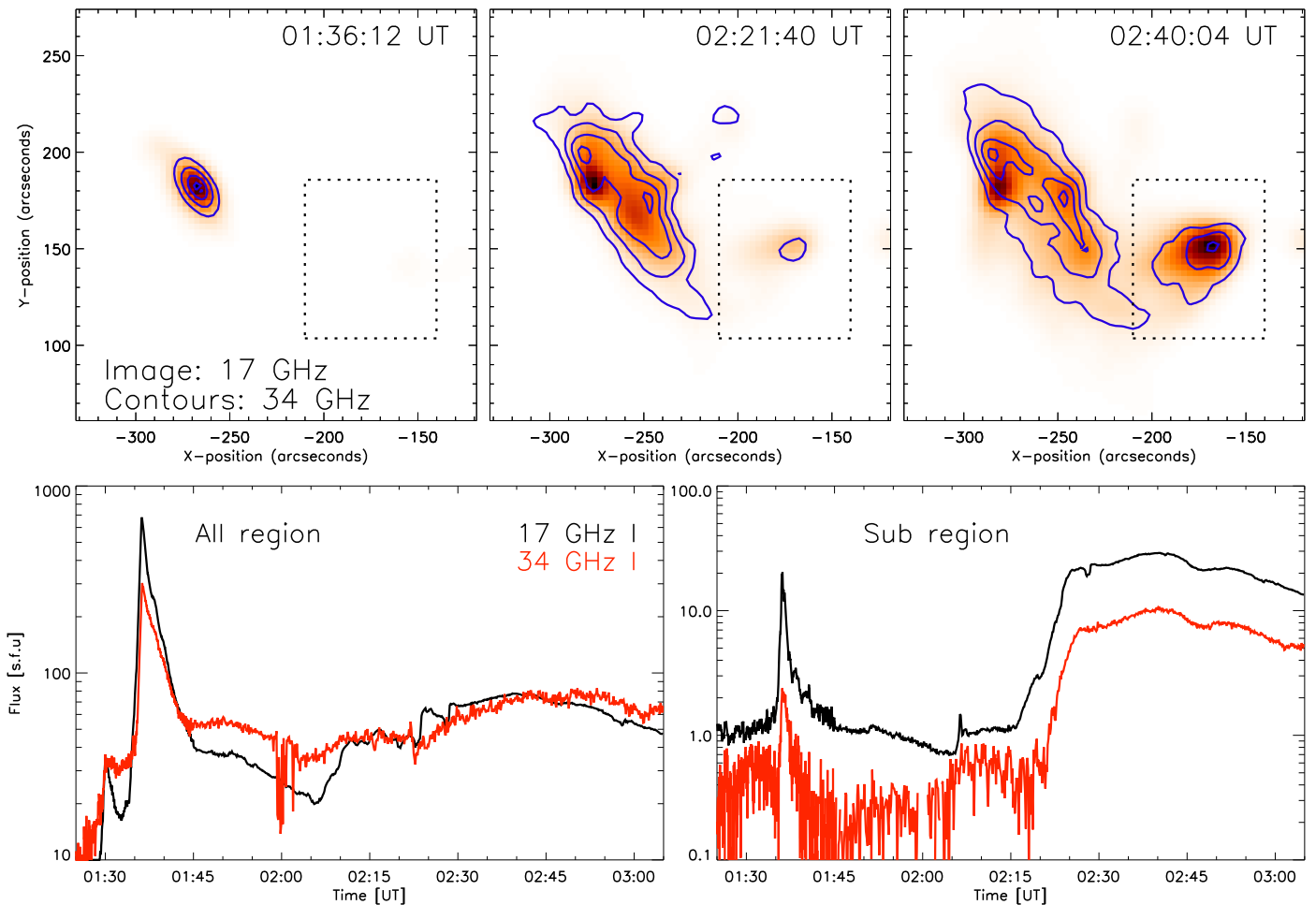
## 2. Time Profiles

Figure 1 shows the soft X-ray light curves from the *Geostationary Operational Environmental Satellite (GOES)* in the top panel and microwave fluxes from the Nobeyama Radio Polarimeters (NoRP) in the bottom panel. Following convention, we use the peak times of the *GOES* soft X-ray flux to denote the two flares as SOL2015-06-21T01:42 (*GOES* class M2.0) and SOL2015-06-21T02:36 (M2.6), respectively. The impulsive flare is a superposition of two impulsive enhancements, with the first

one reaching about M1 level. Also shown as cross symbols are the CME front locations on the C2–C3 coronagraph of the Large Angle Spectroscopic Coronagraph (LASCO) on board *SOHO*, which are published online.<sup>5</sup> The dashed line is a simple linear fit to the LASCO data, which gives the CME speed as  $\approx 1300 \text{ km s}^{-1}$ . Although the NoRP data have typically served as reference flux for solar activities, we found some issues in the calibration at times later than 02:00 UT at frequencies higher than 17 GHz. We thus plot the NoRP data only up to 9.0 GHz, and construct more accurate local flux time profiles from the NoRH maps in Figure 2.

The impulsive and long-duration natures of these two flares are clear in the microwave flux time profiles of the NoRP. For instance, the flux at 9.0 GHz reveals two distinct main peaks; the first flare impulsively reached its maximum at  $\sim 01:36$  UT followed by a rapid decay, and the second flare started about 20–30 minutes later, reached its maximum about 50 minutes later, and has a more gradual profile. The lower three frequencies of NoRP show complex activities. The fast varying emission at 1.0 GHz might imply coherent emission. The complex precursor activity of the second flare during 01:50–02:00 UT makes it hard to determine its precise onset time. From the slope of the NoRP light curves, the onset time of the second flare likely lies between 01:50 UT and 02:00 UT. With the simple linear extrapolation of the CME front to the solar surface (one solar radius in the height), we suppose that the CME motion may have begun after the start

<sup>5</sup> [https://cdaw.gsfc.nasa.gov/CME\\_list](https://cdaw.gsfc.nasa.gov/CME_list)



**Figure 2.** Spatially resolved microwave fluxes as constructed from the NoRH maps. Upper panels: the 17 GHz maps are plotted as inverted gray images and 34 GHz maps in contours. The contours are in (10, 30, 60, 90)% of the maximum intensity at each time. The morphology at 34 GHz appears almost identical to that at 17 GHz throughout the whole event. The bottom panels show the flux time profiles at 17 GHz and 34 GHz from the whole FOV (left) and local fluxes integrated over the dotted box denoted in the upper panels (right).

of the second flare, but we will further investigate the possibility of accelerated CME motion using the EUV images in Section 3.

To supplement the high-frequency ( $\geq 17$  GHz) NoRH fluxes, we calculate the equivalent fluxes from the time series of the NoRH maps at 17 and 34 GHz. In the top panels of Figure 2, we show the NoRH maps at three selective times, where the 17 GHz maps are plotted as inverted grayscale images and 34 GHz maps in contours. At the time of the first impulsive peak (01:36:12 UT), a single compact NoRH source appears. At the time of the second flare (after  $\sim 02:20$  UT), a new source emerges in the west, as indicated by the dashed inset box. The local fluxes within the whole field of view (FOV) of this map are plotted in the bottom left panel. These fluxes should correspond to the total flare fluxes, and they exhibit the characteristic of composite flares (Kosugi et al. 1988). On the other hand, the time profiles of fluxes from the dashed inset box (the bottom right panel) are very different from those of the whole-Sun fluxes. Such temporal behavior of the new source has never been identified previously for any composite flares.

Kosugi et al. (1988) used the 17 GHz fluxes and hard X-ray spectra to study the nature of impulsive and extended bursts. For this event, the *Reuven Ramaty High Energy Solar Spectroscopic Imager* (*RHESSI*) missed the impulsive flare, and in the extended flare, the *RHESSI* spectrum hardly extends above 100 keV. As for why it appears as a soft event, we

consider that the *RHESSI* fluxes become very low by the time of the second flare, and *RHESSI* imaging did not even detect the western source (Figure 2 of Lee et al. 2017). It may be that the accelerated electrons are too small in number to manifest themselves in the high-energy part of the spectrum. We instead use the NoRH fluxes available at the two frequencies, as they are more sensitive to energetic electrons. Fortunately, these 17 and 34 GHz sources appear in the same location with almost equal area, and can be regarded as optically thin sources in which case theoretical expression for emissivity is simply applicable. For electrons obeying a power-law distribution  $n(E) \propto E^{-\delta}$ , the optically thin flux varies with frequency as  $\nu^{-(0.90\delta - 1.22)}$  (Dulk & Marsh 1982). At the first impulsive peak, the flux ratio gives the spectral index  $\approx 1.6$ , which corresponds to  $\delta \approx 3.2$ . For the second microwave source (bottom right panel), the spectral index stays at  $\approx 1.4$ , which corresponds to  $\delta \approx 2.9$ . The latter indicates a very hard energy distribution of electrons, and it is one possibility that the second extended burst is due to trapped electrons, as suggested by Kosugi et al. (1988).

### 3. NoRH Sources on AIA Images

We present temporal evolution of the NoRH 17 GHz sources in comparison with the *SDO* AIA images at 171 Å, 304 Å, and

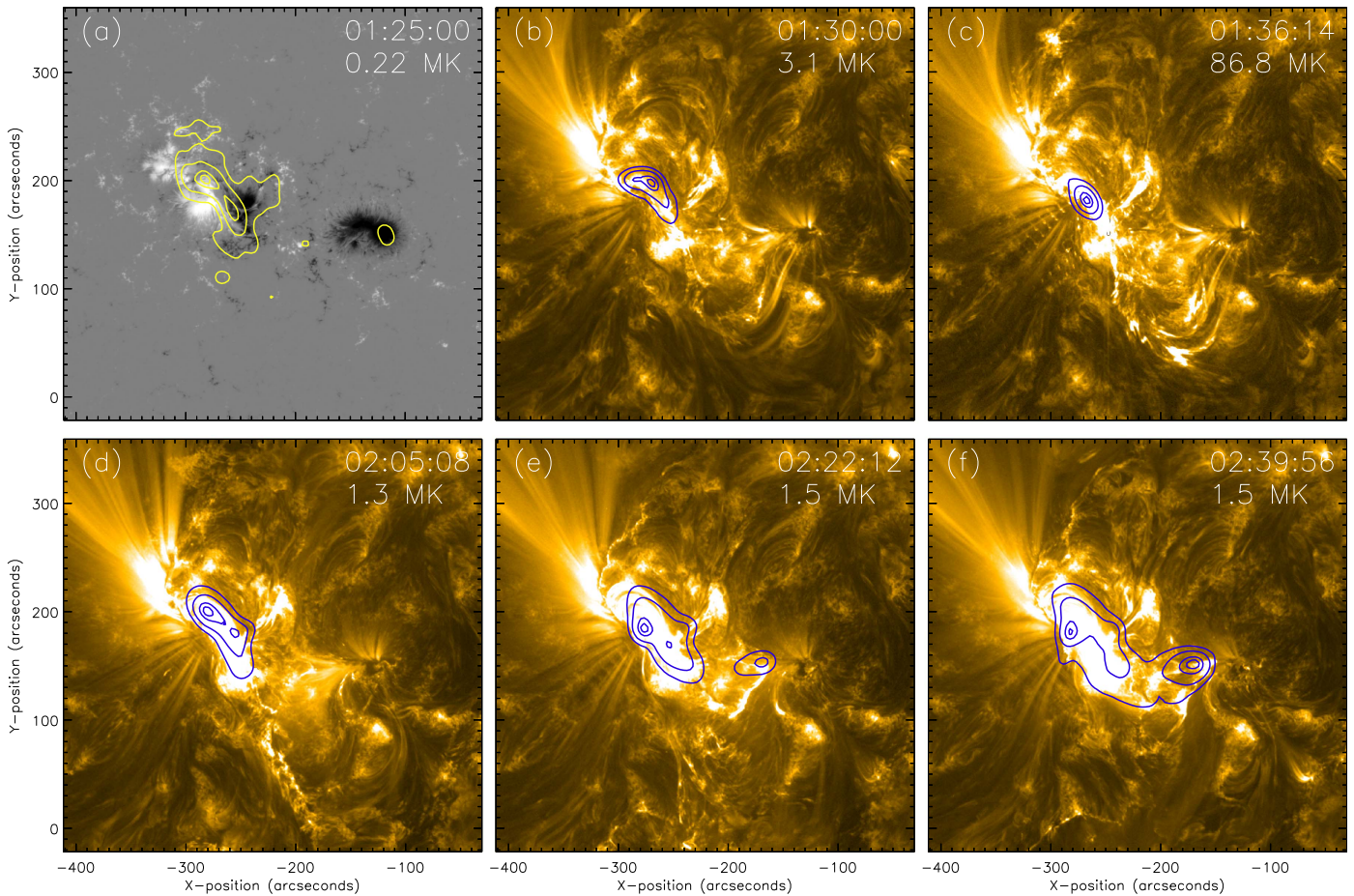


**Figure 3.** NoRH 17 GHz I map (contours) on top of AIA 171 Å images at six time intervals. Only the first panel has the longitudinal HMI magnetogram as background grayscale image. The six time intervals are (a) before the flare (01:25 UT), (b) a precursor activity (01:30 UT), (c) the first flare (01:36 UT), (d) intermission (02:05 UT), (e) start of the second nonthermal microwave source (02:22 UT), and (f) later phase of the second flare (02:40 UT). Contour levels are (10, 30, 70, 90)% of the maximum brightness temperature as denoted in each panel.

(An animation of this figure is available.)

131 Å. The NoRH maps are constructed with an integration time of 2 s and spatial resolution of  $10''$ . All images presented in this section are co-aligned by de-rotating to the location at 01:25 UT. The image quality of NoRH is usually better than 20 dB for typical observations of the quiet Sun (Nakajima et al. 1994). When bright compact sources are present, self-calibration can be used to correct interferometer phase and amplitude errors, leading to much better signal-to-noise ratios (S/N). S/N above 2000 have been achieved in the total intensity at the peak time of the first flare, and after 01:45 UT, S/N values are consistently around 500.

### 3.1. 17 GHz Maps on 171 Å Images

Figure 3 shows the total intensity maps of the NoRH 17 GHz over the AIA 171 Å images except in the first panel, where the HMI longitudinal magnetogram is used instead. They are shown at six different periods: (a) a preflare time, (b) the first phase of the impulsive flare, (c) the maximum of the impulsive flare, (d) an intermission between the two flares, (e) the rise phase of the long-duration flare, and (f) the main phase of the long-duration flare. As shown in the first panel, the source region, NOAA AR 12371, consists of one bipolar spot group in the east and a unipolar spot with negative magnetic polarity in

the west. In that configuration, we can generally expect two magnetic connectivities: one short connection within the bipolar spot group and longer connections between the positive polarity within the bipolar spot group and the distant unipolar spot. It is likely that these two magnetic field connectivities are involved with the two successive flares appearing in the light curves (Figures 1–2), but a more complicated scenario will be found to be the case.

At the preflare time, the 17 GHz NoRH emission appears strong above the magnetic polarity inversion line (PIL) of the eastern bipolar region. Both phases of the impulsive flare (b)–(c) are from a compact source lying over the PIL of the bipolar sunspot. Considering the high dynamic range, this simple structure is not just due to the sensitivity limit, but a real concentration of the high-energy electrons into a compact region narrower than  $10''$ , considering the spatial resolution of the NoRH 17 GHz maps. After the first burst, the source diminishes in intensity and becomes elongated along the PIL (d). It was a surprising result that an additional microwave source appears near the western spot during the second flare at  $\geq 02:10$  UT (e). This source suddenly pops up in a region where no emission in either microwaves or (E)UV was seen previously, and expands with time while maintaining its morphology through the decay phase of the second flare (f).

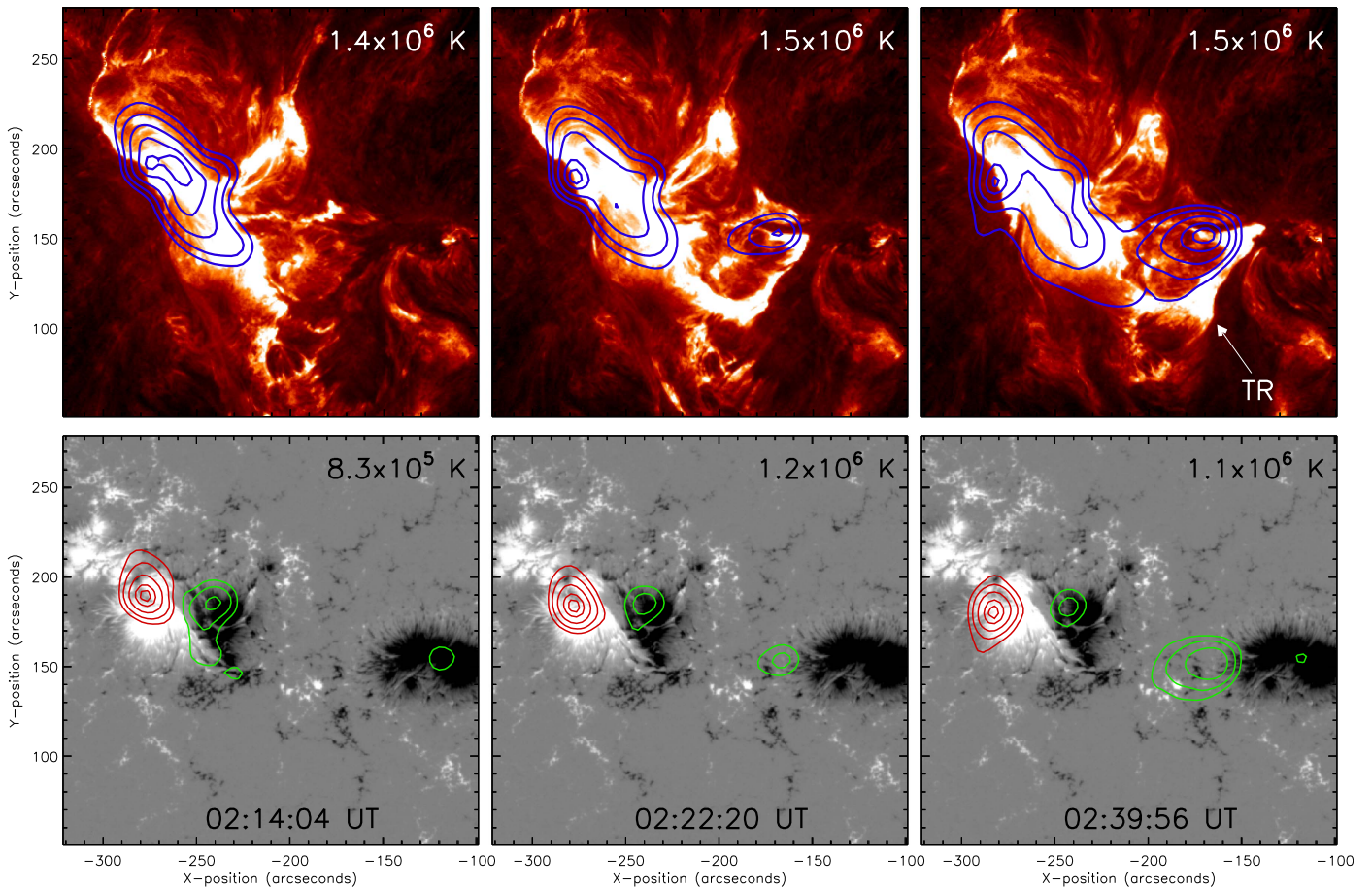


**Figure 4.** NoRH 17 GHz I map (contours) on top of AIA 304 Å (top) and NoRH 17 GHz V map (contours) on a HMI longitudinal magnetogram (bottom) at three times during the second flare. The blue contours represent total intensity and the red (green) contours represent RCP (LCP). Contour levels are (10, 20, 40, 70, 90)% of the maximum brightness temperature as denoted in each panel. TR in the upper right panel indicates the triangular ribbon discussed in the text.

(An animation of this figure is available.)

### 3.2. 17 GHz Maps on 304 Å Images

In Figure 4, we compare the 17 GHz intensity and polarization morphology during the long-duration flare with the UV ribbons shown by the AIA 304 Å images and the longitudinal magnetic field measured by the Helioseismic and Magnetic Imager (HMI) on board *SDO*. The top panels show the total intensity maps at 17 GHz (contours) on top of 304 Å at three time intervals. The bottom panels display the circular polarization maps at 17 GHz on the HMI longitudinal magnetogram, where the right- (left) hand circular polarization, RHC (LHC), is shown as red (green) contours. The new source growing up in the vicinity of the unipolar spot has the LHC polarization, which implies that the source has magnetic fields of negative polarity. The HMI magnetogram shows that there is a group of small patches in the positive polarity surrounded by the negative-polarity magnetic fields. This implies that the new NoRH 17 GHz source is due to high-energy electrons residing in the negative-polarity field that surrounds the positive-polarity patches.

A noticeable change during the second flare is the development of the unusually shaped and nearly closed ribbon near the unipolar spot in the west. This feature denoted as “TR” in the upper right panel takes a form of an acute triangle pointed toward the unipolar spot, and it actually moves closer to the spot during the second flare. The ribbon is located in the

negative-polarity fluxes surrounding the positive-polarity patches, and coincides with the boundary of the emergent 17 GHz source. The coincidence between the two sources in time and space confirms that this represents another event of energy release via magnetic reconnection, and the LHC polarization at 17 GHz implies that the high-energy electrons precipitate mostly into the negative magnetic polarity regions. Such an evolution of the UV ribbon suggests that the second flare should be associated with an eruptive phenomenon, as will be further discussed in Section 4.

### 3.3. 17 GHz Maps on 131 Å Images

In Figure 5, we compare the NoRH 17 GHz maps with AIA 131 Å images, which represent hotter plasma (Fe XXI,  $\sim 10$  MK) than the 171 Å ( $\sim 0.8$  MK) images (Figure 3). Panel (a) shows that there is only a little filament material located along the short section of the PIL within the bipolar sunspot group at the preflare time (01:25:08 UT). (b) This EUV brightness is confined to a short section and grows toward the first flare. (c) Through the first flare, hot loops extend out both northward and southward in a sigmoidal shape. The sigmoidal shape is not well traced by the cool material, for instance, on the 304 Å and 171 Å images. This implies that hot materials ( $\sim 10$  MK) are involved with the sigmoid, and we call this a hot-channel sigmoid (HCS) as marked by arrows. (d) The HCS has moved

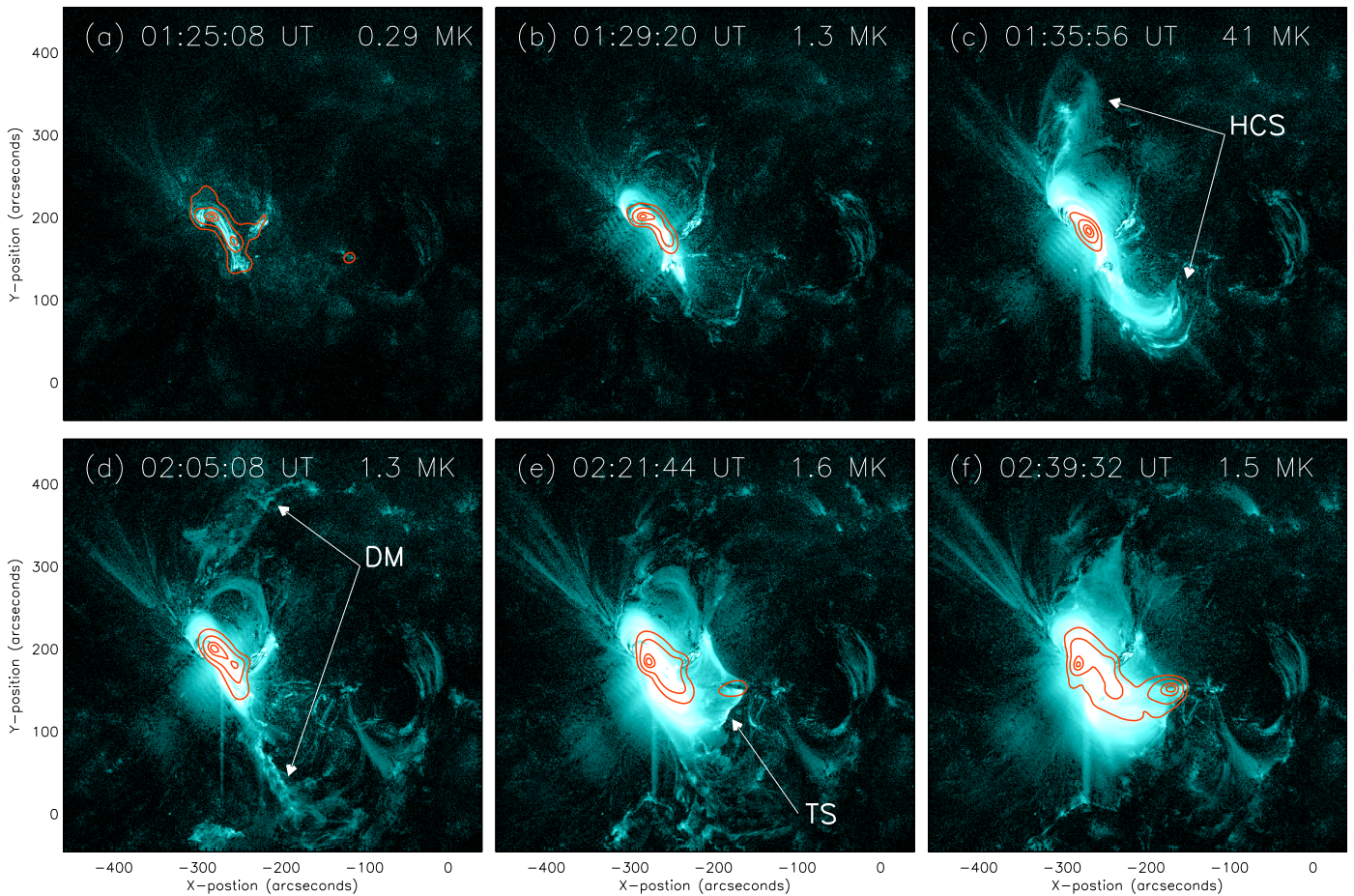


**Figure 5.** NoRH 17 GHz I map (red contours) on top of AIA 131 Å images. (a) Before eruption, the EUV brightness is confined to a short section along the PIL of the bipolar sunspot. (b) The EUV brightening grows toward the first flare. (c) Through the first flare, hot loops extend out both northward and southward to form a hot-channel sigmoid (HCS) as marked by arrows. (d) After the sigmoid has moved out from this FOV by  $\sim 02:04$  UT, EUV bright features remaining are presumably the draining material (DM) along the erupted field lines. (e) After  $\sim 02:20$  UT, bright EUV loops form a triangular structure (TS) over the TR (denoted in Figure 4). (f) The EUV TS becomes more prominent while moving toward the western unipolar spot. These 131 Å images are time-difference images relative to the image at 01:25 UT. The 17 GHz contour levels are (10, 30, 70, 90)% of the maximum brightness temperature as denoted at each panel.

(An animation of this figure is available.)

out from this FOV at  $\sim 02:04$  UT, and is no longer seen by the time of the start of the second flare. Instead, many patchy, transient brightenings are visible, which are presumably the material draining along the erupted field lines. (e) After the eruption, the patchy brightenings disappear and the 131 Å source takes a broader diffuse appearance, which may represent heating in the regions of the erupted flux. The “TR” identified on the 304 Å images (Figure 4) is covered by a bright envelope in a triangular structure (TS), which must consist of hot EUV loops. (f) This feature, TS, unique at 131 Å, becomes more prominent with time and expands toward the unipolar spot, and the accompanying 17 GHz emission is also intensified.

An important aspect of the NoRH observation is that the eastern 17 GHz source coincides with the bright core of the sigmoid, both of which remain stationary during the expansion of the sigmoid. This clearly indicates that the filament eruption associated with the first flare remains confined in space, corresponding well to its impulsive character in the time profile. As a consequence, the bright filament is held down and prevented from growing in height, so that the HCS has to expand in lateral directions until reaching a point of instability for eruption (Figures 5(b), (c)). Another important aspect is that the second 17 GHz source appears during the second flare in

the region coinciding with the location of 304 Å TR and is associated 131 Å TS (Figures 5(e), (f)) The latter two are expanding toward the unipolar spot, which indicates progressive magnetic reconnection in contrast with the first confined reconnection.

#### 4. Magnetic Field Structure

We investigate the magnetic field structure of the source region, NOAA AR 12371, to find out the magnetic characteristics at the locations of the microwave sources, and to explain, if possible, why they could host such an impulsive and a long-duration flares as observed. We use a nonlinear force-free field (NLFFF) extrapolation code developed by Wiegmann (2004) together with a Spaceweather HMI Active Region Patch (SHARP) image as the boundary condition. Initially, we had used three SHARP images taken at 01:22:25 UT, 01:58:25 UT and 02:58:25 UT, which correspond to a preflare period, an intermission between the two flares, and a postflare period, respectively. No significant changes with time were found, except that the high-lying field lines connecting two spots become more relaxed through the flares. We proceed with a single NLFFF model constructed with the SHARP image at 01:22:25 UT, and focus on its static structure.

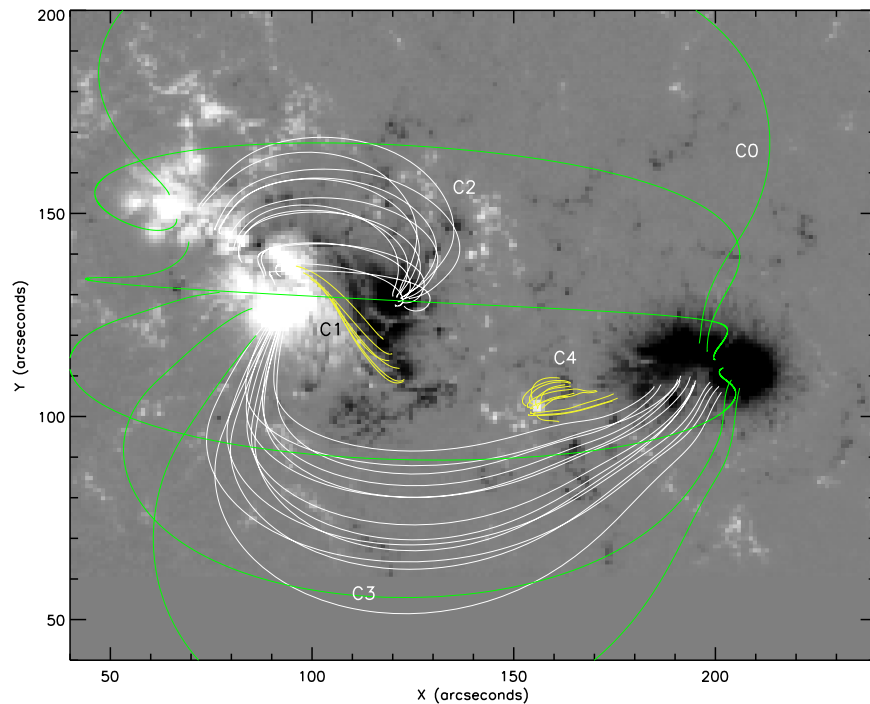


**Figure 6.** Magnetic field lines reconstructed using the NLFFF extrapolation from the SHARP image of NOAA AR 12371. Five major connectivity groups are identified: high-lying field lines over the whole AR (denoted C0), highly sheared along the PIL within the bipolar spot group (C1), connecting the strong negative polarity to the northern part of the positive polarity in the group (C2), connecting the unipolar sunspot to the positive spot in the group to the surrounding positive plage and network flux (C3), and a compact field line group from the positive-polarity flux in the vicinity of the western unipolar spot (C4).

#### 4.1. The AR Field Lines

In Figure 6, we plot selective field lines calculated from the NLFFF model. At the time of this event, NOAA AR 12371 was located near the disk center (approximately N10E17), and the figure shows a nearly top-down view of the AR. The AR consists of a unipolar spot with the negative magnetic polarity, which neighbors the bipolar spot group in the east. Consequently, the field lines connecting the positive-polarity flux in the east to the negative-polarity flux in the west are covering the whole AR, as represented by the group of green lines (denoted C0). These high-lying closed field lines are apparently in the near-potential state and cover both flare sources, making it hard to achieve any eruption from them. Under these high-lying closed fields, there are, at least, four distinct connectivity groups, which we denoted C1–C4. C1 refers to the short compact and highly sheared loops crossing the PIL within the bipolar spot group, and is obviously the source for the first impulsive flare, as these field lines run between the prominent ribbons of the flare. C2 consists of the longer field lines connecting the positive and negative fluxes within the bipolar spot group running north, which is partly seen in EUV images in the later phase as hot loops. C3 connects the positive flux in the bipolar spot group to the negative unipolar spot, which is occasionally visible during the eruption. With increasing height, C2 gradually joins C3 to form the high-lying field lines, C0, covering the whole AR. C3 is therefore equivalent to C0 in topology. C4 consists of the scattered positive-polarity patches connected to the surrounding negative-polarity patches in the vicinity of the western unipolar spot. C4 is likely to be associated with the second microwave source. Both C1 and C4 are confined by the overlying C2, C3, and C0, as can be seen in Figure 6. It is important to note that according to this NLFFF model, the field lines in C2 and lower part of C3, which pass

over the initially erupting flux C1, are considerably sheared compared with the higher lying field lines, C0. As they carry significant current and free magnetic energy, they are capable of eruption upon adequate perturbations.

In Figure 7, we focus on the fine structures in C1 and C4, where the first and the second microwave sources are located, respectively. In the left panel, we again find all field lines in C1 running nearly parallel to the PIL. We can, however, distinguish two groups in color: the blue field lines (denoted C1) connecting the negative-polarity flux in the center of the bipolar spot to the northern conjugate footpoints, and the red lines (C1\*) connecting the positive-polarity flux in the center of the spot to the southern conjugate footpoints. The connectivity in the center of the spot therefore changes very rapidly across the PIL, which means that a magnetic separatrix should exist between C1 and C1\*. This is a place where flaring is highly feasible, but the impulsiveness of the first flare from this location means that the magnetic reconnection occurred in a highly confined condition. The right panel shows the field lines in C4 (red) and those in C3 (blue). The C3 field lines connect the positive flux of the bipolar spot to the unipolar spot in the west running over C4, and this connectivity continues with height. With decreasing heights, however, the same connectivity cannot be maintained because of the positive polarity present on the way, so that these low-lying field lines (denoted C3\*) end up on the negative-polarity patches lying east of the positive-polarity patches, instead of crossing over them. As a result, the connectivity steeply changes at the location where C3, C3\*, and C4 adjoin each other. This is the place where a magnetic null point may actually exist, and magnetic reconnection may occur when perturbed by the overlying fields in C3. Upon such magnetic reconnection, high-energy electrons are accelerated and fan out along the dome-like separatrix (red lines) to precipitate toward its footpoints. This

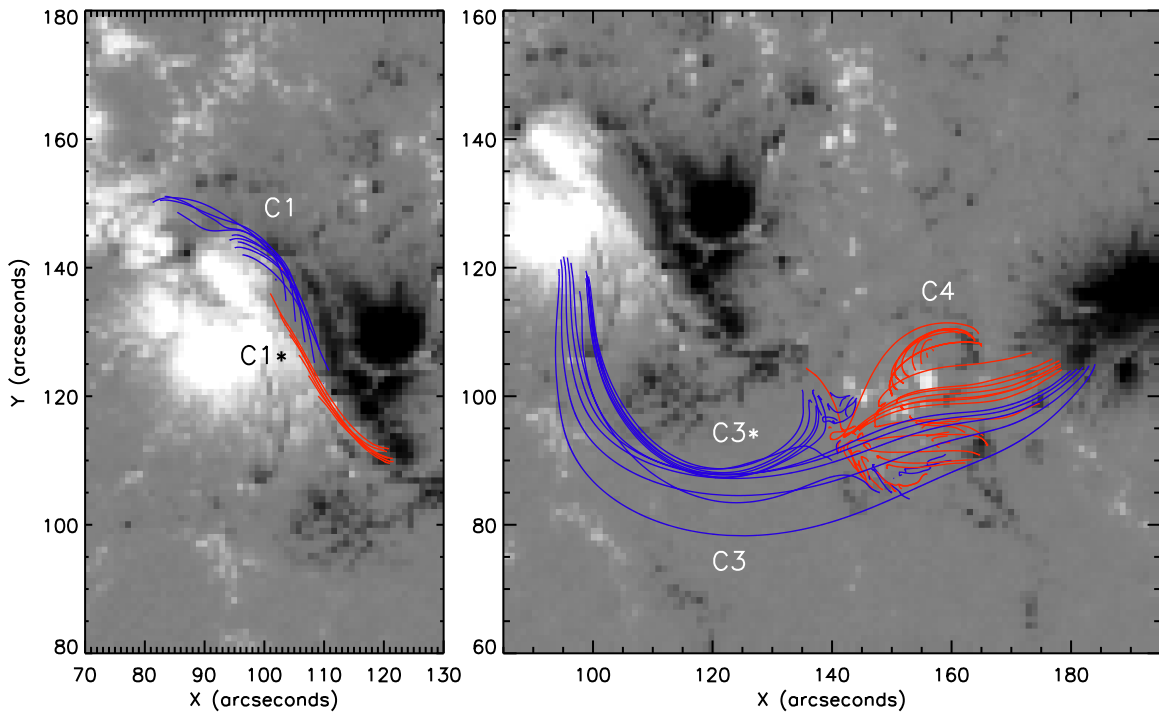


**Figure 7.** Magnetic field lines involved with the flaring. Left panel shows C1 field lines which are lower-lying, sheared along the PIL within the bipolar spot group. Here, lines starting from the positive polarity (red) are distinguished from the negative-polarity region (blue) in color. Right panel shows three connectivity groups around the second flare source, C4. The blue colored field lines are in two connectivities: the field lines in the aforementioned C3 connect the two spots running above C4. At lower heights, however, the field lines starting from the positive flux connect themselves to the negative flux in the middle of the two spots, which is denoted as C3\*. C4 is a dome-like separatrix (red) formed by the positive-polarity flux surrounded by negative flux patches.

can explain the unusual appearance of the triangular EUV ribbons around C4 (Figures 3–4).

#### 4.2. Quasi-separatrix Layers

We further search for the locations of the Quasi-Separator Layers (QSLs), where the magnetic connectivity has a high gradient, thus magnetic reconnection tends to occur upon perturbations of magnetic equilibria (e.g., Démoulin et al. 1996; Aulanier et al. 2005). Such QSL locations have typically been compared with those of flare ribbons observed at H $\alpha$  and (E)UV lines, but here we attempt such a comparison with the microwave sources. The best known measure for identifying QSLs is the squashing factor  $Q$ , which can be calculated using a mapping of two footpoints of a field line:  $\mathbf{r}_1(x_1, y_1) \mapsto \mathbf{r}_2(x_2, y_2)$  in the following manner (Titov & Hornig 2002; Titov et al. 2002):

$$Q \equiv \frac{a^2 + b^2 + c^2 + d^2}{|B_{n,1}(x_1, y_1)| |B_{n,2}(x_2, y_2)|} \quad \text{where} \quad \begin{pmatrix} a & b \\ c & d \end{pmatrix} \equiv \begin{pmatrix} \partial x_2 / \partial x_1 & \partial x_2 / \partial y_1 \\ \partial y_2 / \partial x_1 & \partial y_2 / \partial y_1 \end{pmatrix}, \quad (1)$$

where  $B_{n,1}$  and  $B_{n,2}$  are the magnetic field components normal to the plane of the footpoints, i.e., the photosphere. To perform this calculation of  $Q$ , we use the code developed by Liu et al. (2016). By convention, we apply this calculation to the potential field model instead of the more realistic NLFFF model because the latter presents too complex structure to provide a clear picture, while there is no essential difference.

Figure 8 shows the calculated maps of  $Q$ . As this quantity varies to a large extent, we plot only  $Q$  in the range of

$10^2 \leq Q \leq 10^5$  in logarithmic scale. The left panel shows  $Q$  on the  $x$ - $y$  plane at height of  $2''5$ , and the right panels,  $Q$  on the two distance-height planes along the two slits, shown as dashed lines, S1 and S2, in the left panel. At the low coronal height, these  $Q$  values are concentrated within the narrow lanes (left panel), whereas at greater coronal heights, they may appear more dispersive (right panels). These  $Q$  maps reveal traces of a few closed QSLs, and of particular interest is the QSL indicated by an arrow in each panel, which actually defines the border of C4 and thus the region of the second microwave source. Since the part of the closed QSL of C4 matches the triangular UV ribbon (Figure 3), we can take the ribbon’s brightening around 02:15 UT as implying that the energetic electrons precipitate down to the chromosphere along this QSL. Note also that this QSL boundary lies above the negative magnetic polarity, consistent with the observed LHC polarization of the 17 GHz source (Figure 4).

The two right panels reveal that the QSL associated with C4 has a dome-like structure confined to relatively low heights, which is also implied by the field lines shown in the right panels of Figure 7. We argue that the eruption associated with the CME must have occurred in the high-lying field over C4. As a result, re-arrangement of the field lines occurring in the space above C4 would induce the expansion and shift of the QSL, C4, but without destroying it. In this case, the observed motion of the triangular ribbon (see the animation accompanying Figure 4) implies the expansion of the QSL toward the western spot, undergoing magnetic reconnection with adjacent fluxes outside of C4. It is plausible that such motion is driven by the continuous rise of the reconnected part of C3. As a closed QSL, C4 is also an ideal space for the trapping the high-energy electrons, thus explaining why the second nonthermal source occurring there has an extended time profile.

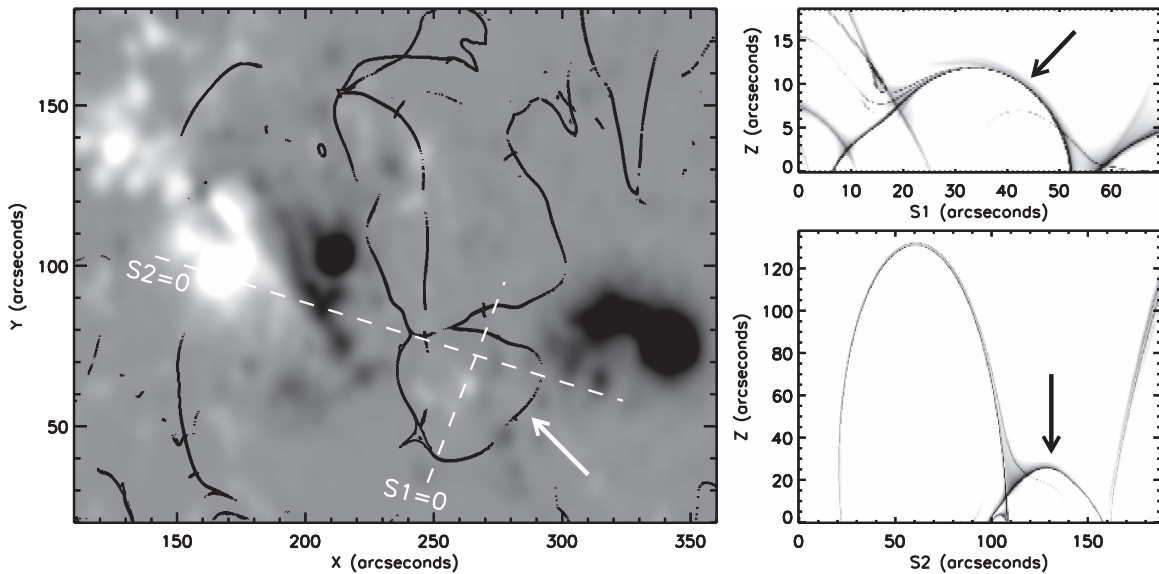


**Figure 8.** Magnetic separatrix layers. The left panel shows a map of  $Q$  on the  $x$ - $y$  plane at the height of  $z = 2''5$  plotted against the HMI longitudinal magnetogram at 01:25:30 UT. The two right panels show the height distribution of  $Q$  scanned along the slit denoted in the left panel. Only high  $Q$  values are plotted as a trace for separatrix layers. In each panel, the separatrix of C4 is indicated by an arrow.

#### 4.3. A Scenario for Eruption

We make a couple of inferences on the eruption with the above results, although the force-free field model does not directly address the eruption itself. This includes results from a detailed study of the impulsive flare and HCS in Kliem et al. (2018). During and around the first flare, the field lines near the PIL reconnect under the middle of the filament in C1 (yellow lines in Figure 6) to supply more flux to the sigmoid as in the process proposed by van Ballegoijen & Martens (1989) or Green et al. (2011). Increase in the length of the sigmoid should induce a growth in height. According to the NoRH observation, however, the microwave source and thus the region of primary energy release remains confined and stationary, in which case the sigmoidal elbow is forced to expand laterally (Figure 5(c)). When it reaches a point of instability, the HCS would then have evolved directly into the fast halo CME observed by LASCO/C2. The magnetic reconnection during the first flare enhances the magnetic flux rope in a manner topologically equivalent to tether-cutting reconnection. A difference is that the flare reconnection is a fast process whereas the tether-cutting reconnection is originally suggested to be slow.

The aforementioned rise of the field lines in C3 is neither observed nor modeled in this study. It is only speculated based on the observed eruption of the HTS. Such eruption could have perturbed the magnetic equilibria in C4 to steepen the current density and enhance the dissipation in the QSL (e.g., Démoulin et al. 1996; Aulanier et al. 2005). This explains the (E)UV brightenings occurring along the whole QSL encircling C4 after  $\sim 02:15$  UT. The brightening is located in the north-western side of the QSL C4 and moves in the northwest direction (see Figures 3–4 and associated animations), which indicates that magnetic reconnection continued between the QSL in C4 and the surrounding magnetic flux to expand in that direction. This will also make the overlying field lines in C3 longer, and necessarily induces the rise of C4. This type of reconnection can slowly continue, while the QSL of C4 itself essentially remained closed. It follows that the eruption of the field lines in C2 and C3 is the key driver of the second flare.

This scenario describes a continuous transition from the first to the second flare, consistent with the X-ray and radio light curves, and the seamless motions seen in the EUV images through the whole composite flare.

While the present analysis is focused on the core of the NOAA AR 12371, it will be appropriate to compare our conclusion with a recent study where involvement of a large-scale magnetic structure in this eruption is emphasized (Lim et al. 2017). Around this AR, a large closed magnetic structure forms, because the unipolar spot with the negative magnetic polarity is neighbored not only by the bipolar spot group in the east (as presented in this paper) but by the adjacent large coronal hole (CH) of positive magnetic polarity in the west (not shown in this paper). Consequently, the two negative-polarity spots provide a central region surrounded by positive-polarity fluxes on the east and west sides, in which case the closed AR field lines and the surrounding open field lines of the CH form a large pseudo streamer structure. One of the highlights of Lim et al.'s (2017) study is the observation of EUV brightenings running along the long arc encircling the AR, which would correspond to the footpoints of the pseudo streamer. They found the motion temporarily correlated with the second flare and regarded it as evidence for the second flare being associated with the disturbance over such a large area. This EUV motion is the most apparent in AIA 304 Å, and less in higher temperature EUV lines with no counterpart at either microwaves or hard X-rays. Nevertheless our interpretation requires a large-scale disturbance occurring above the AR due to the eruption of the sigmoid, which incurs a perturbation of the small separatrix dome underneath and subsequent magnetic reconnection for the second microwave burst in succession. The second microwave source can therefore be regarded as one of the effects of such a large-scale disturbance.

## 5. Conclusion

We have presented the first imaging analysis of a composite microwave burst during two flares, SOL2015-06-21T01:42 (M2.0) and SOL2015-06-21T02:36 (M2.6) in NOAA AR

12371 near disk center. A detailed investigation of the event using a data set from *SDO*, NoRH, and an NLFFF model is performed to address the specific question as to how the various components of the first, impulsive and second, longer-lasting flare can be understood, and how they are related to each other. Our findings are summarized as follows:

1. The first microwave burst is confined in time and in space, as evidenced by the associated confined eruption of a filament, from the stagnation of ribbon separation and their simultaneous moderate fading between the two flares, from the absence of significant further acceleration of particles in the source region until the second flare, and from the stationarity of the eastern microwave source. This implies that the first reconnection above the low-lying, highly twisted field lines could not proceed upward due to the strongly suppressing, overlying fields.
2. Nevertheless, the flare contributed to the rapid growth of the HCS. The HCS continued to grow even after the first flare, albeit at a lower rate. The HCS expanded until it reaches a point of instability after which it erupted. The way that the impulsive, confined flare enhanced the magnetic flux rope is similar to the tether-cutting reconnection. A difference is that the former is a fast reconnecting process whereas the latter is originally suggested to be slow. However, they are topologically equivalent to each other.
3. The subsequent special phenomenon of a nearby closed, triangular flare ribbon, which forms in the main phase of the second flare, coincides with the second microwave source. This microwave source can be explained by postulating the perturbation of the closed QSL dome of an isolated parasitic polarity, caused by the rise of its overlying magnetic flux. The large-scale restructuring of the coronal magnetic field originates from the sigmoid eruption in which the first flare plays a role of tether cutting, and the second microwave burst is one of the effects.

The suggested scenario explains how the first microwave burst is related to the much-delayed second microwave burst in this composite event.

This work was carried out in the framework of the joint research program at the Institute for Space-Earth Environmental Research (ISEE), Nagoya University. J.L. and B.K. acknowledge the invitation by ISEE to join the program. B.K.

also acknowledges support by ISSI, Bern for the International Team “Decoding the Pre-eruptive Magnetic Configuration of CMEs” and support by the DFG and by NASA under grants NNX16AH87G and 80NSSC17K0016. C.L. is supported by NASA grants NNX13AF76G, NNX16AF72G, and 80NSSC17K0016. S.W. was supported by an AFOSR Windows on the World grant. Nobeyama Radioheliograph is operated by the International Consortium for the Continued Operation of Nobeyama Radioheliograph (ICCON). ICCON consists of ISEE/Nagoya University, NAOC, KASI, NICT, and GSFC/NASA.

### ORCID iDs

Jeongwoo Lee  <https://orcid.org/0000-0002-5865-7924>  
 Stephen M. White  <https://orcid.org/0000-0002-8574-8629>  
 Chang Liu  <https://orcid.org/0000-0002-6178-7471>  
 Bernhard Kliem  <https://orcid.org/0000-0002-5740-8803>

### References

- Alfvén, H., & Carlqvist, P. 1967, *SoPh*, **1**, 220  
 Andrews, M. D. 2003, *SoPh*, **218**, 261  
 Aulanier, G., Pariat, E., & Démoulin, P. 2005, *A&A*, **444**, 961  
 Bai, T., & Sturrock, P. A. 1989, *ARA&A*, **27**, 421  
 Démoulin, P., Henoux, J. C., Priest, E. R., & Mandrini, C. H. 1996, *A&A*, **308**, 643  
 Dulk, G. A., & Marsh, K. A. 1982, *ApJ*, **259**, 350  
 Green, L. M., Kliem, B., & Wallace, A. J. 2011, *A&A*, **526**, A2  
 Kai, K., Nakajima, H., Kosugi, T., & Kane, S. R. 1983, *SoPh*, **86**, 231  
 Kai, K., Nakajima, H., Kosugi, T., Stewart, R. T., & Nelson, G. J. 1986, *SoPh*, **105**, 383  
 Kane, S. R. 1969, *ApJL*, **157**, L139  
 Kliem, B., Lee, J., White, S. M., Liu, C., & Masuda, S. 2018, *ApJ*, submitted  
 Kosugi, T., Dennis, B. R., & Kai, K. 1988, *ApJ*, **324**, 1118  
 Kosugi, T., Kai, K., & Suzuki, T. 1983, *SoPh*, **87**, 373  
 Lee, J., White, S. M., Jing, J., et al. 2017, *ApJ*, **850**, 124  
 Lemen, J. R., Title, A. M., Akin, D. J., et al. 2012, *SoPh*, **275**, 17  
 Lim, E.-K., Yurchyshyn, V., Kumar, P., et al. 2017, *ApJ*, **850**, 167  
 Liu, R., Kliem, B., Titov, V. S., et al. 2016, *ApJ*, **818**, 148  
 Nakajima, H., Dennis, B. R., Hoyng, P., et al. 1985, *ApJ*, **288**, 806  
 Nakajima, H., Enome, S., Shibasaki, K., et al. 1994, *Proc. IEEE*, **82**, 705  
 Pallavicini, R., Serio, S., & Vaiana, G. S. 1977, *ApJ*, **216**, 108  
 Shibata, K., & Magara, T. 2011, *LRSP*, **8**, 6  
 Titov, V. S., & Hornig, G. 2002, *AdSpR*, **29**, 1087  
 Titov, V. S., Hornig, G., & Démoulin, P. 2002, *JGR*, **107**, 1164  
 Uchida, Y., & Shibata, K. 1988, *SoPh*, **116**, 291  
 van Ballegooijen, A. A., & Martens, P. C. H. 1989, *ApJ*, **343**, 971  
 Wiegmann, T. 2004, *SoPh*, **219**, 87  
 Wild, J. P., Smerd, S. F., & Weiss, A. A. 1963, *ARA&A*, **1**, 291  
 Yashiro, S., Akiyama, S., Gopalswamy, N., & Howard, R. A. 2006, *ApJ*, **650L**, 143